Asia-Pacific Journal of Atmospheric Sciences (2019) 55:589–608
https://doi.org/10.1007/s13143-019-00104-1

Online ISSN 1976-7951
Print ISSN 1976-7633

ORIGINAL ARTICLE

Gravity Waves Associated with Jet/Front Systems. Part I: Diagnostics and their Correlations with GWs Revealed in High-Resolution Global Analysis Data

Hye-Yeong Chun[1] · Byeong-Gwon Song[1,2] · Seok-Woo Shin[3] · Young-Ha Kim[4]

Received: 10 August 2018 / Revised: 29 December 2018 / Accepted: 11 January 2019 / Published online: 15 February 2019

Abstract

Jet/front systems are the important sources of the atmospheric gravity waves (GWs). Based on mesoscale simulation results, dominant GWs associated with the jet/front systems have horizontal wavelengths of approximately 150 km, which need for parameterization in global models. Nevertheless, there is no comprehensive parameterization scheme of the jet/front GWs with a formulation of the GW momentum flux (GWMF) at launch level, due primarily to uncertainties in their generation mechanisms. In this study, we evaluate two diagnostics of the jet/front GWs, frontogenesis function (FF) and residual of the nonlinear balance equation (RNBE), by examining their spatiotemporal variations using two global reanalysis data sets over 32 years (1980–2011) and by examining correlations between the diagnostics and the GWMF resolved from high-resolution global analysis data in January and July of 2007. The FF and RNBE are maximal in the mid-to-high latitudes of the winter hemisphere, with local maxima in Greenland, East Asia, western North America, Antarctic Peninsula, and the Andes Mountains. The GWMF is dominant in two regions in the upper troposphere: (i) poleward of 30° in both hemispheres, with a larger value in the winter hemisphere, and (ii) tropical and subtropical regions in both hemispheres. The FF and RNBE are well correlated with the GWs in the mid-to-high latitudes following their seasonal variations, which successfully separate GWs in the tropics and subtropics generated by convective sources. In Part II, a parameterization based on the RNBE is developed and implemented in a climate model, and its impacts on the large-scale flow will be investigated.

Keywords Jet/frontal systems · Gravity waves · Frontogenesis function (FF) · Residual of nonlinear balance equation (RNBE) · Gravity-wave parameterization

1 Introduction

Atmospheric gravity waves (GWs) are generated by various sources in the troposphere, such as topography, convection, jet/front systems, density impulse, and shear instability. Vertically propagating GWs contribute significantly to the wind and temperature of the middle atmosphere, where waves are dissipated mostly through wave-breaking, critical-level filtering, and diffusion processes (Lindzen 1981). In the mesosphere, updraft in the summer polar region and downdraft in the winter polar region in a one-cell meridional gyre induced by GW drag (GWD) produce the observed temperature, which is significantly different from the radiative equilibrium temperature (Andrews et al. 1987; Garcia and Boville 1994; Fritts and Alexander 2003). In the stratosphere, GWs contribute to the Brewer-Dobson circulation (BDC) along with planetary waves (Randel et al. 2008; Chun et al. 2011; Polichtchouk et al. 2018).

Responsible Editor: Soon-Il An.

✉ Hye-Yeong Chun
chunhy@yonsei.ac.kr

[1] Department of Atmospheric Sciences, Yonsei University, 50 Yonsei-ro, Seodaemun-gu, Seoul 03722, South Korea

[2] Division of Polar Climate Sciences, Korea Polar Research Institute, Incheon, South Korea

[3] Climate Research Division, National Institute of Meteorological Sciences, Jeju, South Korea

[4] Institut für Atmosphäre und Umwelt, Goethe Universität Frankfurt, Frankfurt am Main, Germany

Recent climate change simulations have revealed that the contribution of GWs to the BDC is even larger than that by planetary waves in the changing climate (Butchart and Coauthors 2010). There is, however, a question is raised by Cohen et al. (2013) whether partitioning the forcing by planetary waves and GWs separately to the BDC is meaningful, suggesting a compensation mechanism between the two wave forcing.

Among various sources of GWs in the troposphere, topography, convection, and jet/front systems are known to be the major sources. Unlike the topographic and convective GWs of which GWD parameterizations have been developed actively during the last 20–30 years, GWs associated with jet/front systems have been studied relatively recently, and the generation mechanisms through which the GWs are associated with jet/front systems remain an active area of current research and debate (Plougonven and Zhang 2014). The generation mechanisms of the jet/front GWs proposed in the literature are (i) geostrophic adjustment, (ii) Lighthill radiation, (iii) unbalanced instability, and (iv) transient generation by sheared disturbance. The classical geostrophic adjustment explains the emission of GWs in an initially imbalanced flow from the geostrophy, with the spatial scales that depend on the prescribed perturbation (or imbalance). Although the geostrophic adjustment has been proposed as a generation mechanism of GWs near jet/front systems (e.g., O'Sullivan and Dunkerton 1995), it is difficult to explain the continuous emission of waves and persistent imbalance after the appearance of waves that were evidenced from high-resolution numerical modeling studies (e.g., Wang and Zhang 2010). This situation is properly termed "spontaneous balance adjustment" or "spontaneous adjustment emission" (Ford et al. 2000; Wang and Zhang 2010). The other three mechanisms generally represent spontaneous emission processes. Lighthill radiation provided a first clear view of the emission of GWs from the balanced flow during their evolution, with horizontal scales larger than the balanced flow. Unbalanced instabilities and transient generation mechanisms describe how shear couples GWs and balanced motions, leading to emissions in the form of unstable modes or transient bursts. Details of each mechanism and references can be found in Plougonven and Zhang (2014).

Since the work by Uccelini and Koch (1987), there have been several observational studies on the GWs associated with jet/front systems based on radiosondes, radars, aircraft measurements, super-pressure balloons, and satellites (e.g., Fritts and Nastrom 1992; Eckermann and Vincent 1993; Sato 1994; Guest et al. 2000; Plougonven and Teitelbaum 2003; Wang and Geller 2003; Wu and Zhang 2004; Zhang and Yi 2007; Hertzog et al. 2008; Ern et al. 2011; Ki and Chun 2011). Based on observational studies, the GWs associated with jet/front systems have horizontal wavelengths of 50–500 km, vertical wavelengths of 1–4 km and periods of 0.5–4 h, with pressure perturbation of approximately 0.5–15 hPa at the surface. Since O'Sullivan and Dunkerton (1995), numerical modeling studies using relatively high-resolution global or regional mesoscale models have been conducted (e.g., Zhang 2004; Plougonven and Snyder 2007; Wang and Zhang 2007; Wu and Eckermann 2008; Shutts and Vosper 2011; Sato et al. 2012; Zhang et al. 2013; Kim et al. 2016). The horizontal and vertical resolutions of the models used from the aforementioned numerical modeling studies range from ~10 km to ~100 km and from ~125 m to ~600 m, respectively. Based on the mesoscale numerical modeling results by Zhang (2004) with horizontal and vertical resolution of 10 km and 360 m, respectively, GWs that have horizontal wavelengths of approximately 150 km, vertical wavelengths of approximately 2.5 km, periods of approximately 4f (f is Coriolis parameter), and phase speeds of approximately 8 m s^{-1} are dominant, which are generated in the exit region of the upper-level jet stream. Comprehensive reviews of the observational and modeling studies of the GWs associated with the jet/front systems and references can also be found in Plougonven and Zhang (2014).

The dominant GWs associated with the jet/front systems with the horizontal wavelengths of about 150 km are not fully resolved from most current GCMs and should be parameterized. The parameterization of GWs associated with jet/front systems for use in a GCM was first proposed by Charron and Manzini (2002) in the middle-atmosphere extension version of ECHAM4 (MAECHAM4). They calculated the frontogenesis function (FF) at 600 hPa and launched GWs at the grids where FF is larger than a certain threshold, with the uniform momentum flux having a Gaussian-type distribution with respect to phase speed. This GWD scheme has been used in the Whole Atmosphere Community Climate Model (WACCM) by Richter et al. (2010) and a global weather forecasting model by Choi et al. (2018). Recently, Mirzaei et al. (2014) proposed an empirical parameterization of IGWs associated with jet/front systems, including moist convection.

The frontal GWD parameterization used in Richter et al. (2010) and Choi et al. (2018) is somewhat primitive compared with orographic and convective GWD schemes of which the launch-level momentum flux spectrum is determined explicitly based on the analytical formulation of the linear GWs forced by topography and diabatic heating of convective clouds, respectively. However, it is still better than commonly used background non-orographic GWD parameterizations that assign the GW momentum flux uniformly without explicitly considering GW sources. Therefore, before comprehensive GWD parameterizations of the jet/front GWs are developed, jet/front GWD parameterizations based on proper diagnostics need to be examined and updated. Note that any comprehensive GWD parameterization scheme requires a formulation of the momentum flux spectrum at source location based on the GW generation mechanism, while the GWD parameterization based on proper diagnostics only can select a location of potential wave source, without the momentum flux information there. One alternative diagnostic of GWs

associated with jet/front systems, in addition to the FF that is currently used in WACCM, is the residual of the nonlinear balance equation (RNBE) proposed by Zhang (2004), which has been used in several studies on GWs and aviation turbulence (e.g., Sharman et al. 2006; Sato and Yoshiki 2008; Ki and Chun 2011; Kim et al. 2011; Limpasuvan et al. 2011; Murphy et al. 2014; Song et al. 2017).

In the present study, we will examine the spatiotemporal variations in the FF and RNBE using two 32-year global reanalysis data sets, and then the validity of the FF and RNBE as diagnostics of GWs associated with jet/front systems is examined based on their correlations with the GW momentum flux (GWMF) estimated from high-resolution global analysis data. In section 2, formulations of the FF and RNBE are given in the spherical coordinates. In section 3, the reanalysis datasets used in the present study are described and the spatiotemporal variations in the FF and RNBE will be given. In section 4, the GWMFs estimated from the high-resolution global analysis data at three selected levels (300, 70, and 5 hPa) in January and July of 2007 are provided, and their correlations with the FF and RNBE will be presented in section 5. Summary and conclusion are given in the last section. In Part II, a new parameterization based on RNBE is implemented into WACCM, and its impact on the large-scale flow will be examined.

2 Formulations of the FF and RNBE in Spherical Coordinates

2.1 Frontogenesis Function (FF)

Frontogenesis occurs when strong deformation tends to increase horizontal temperature gradient, and the evolution of the horizontal temperature gradient can be expressed by the FF (Hoskins 1982). When vertical motion, diabatic effects, and diffusion are neglected, a two-dimensional FF can be given, following Charron and Manzini (2002):

$$FF \equiv \frac{1}{2}\frac{D}{Dt}|\nabla\theta|^2 = -\left(\frac{1}{a\cos\phi}\frac{\partial\theta}{\partial\lambda}\right)^2\left(\frac{1}{a\cos\phi}\frac{\partial u}{\partial\lambda}-\frac{v\tan\phi}{a}\right)-\left(\frac{1}{a}\frac{\partial\theta}{\partial\phi}\right)^2\left(\frac{1}{a}\frac{\partial v}{\partial\phi}\right) -\left(\frac{1}{a\cos\phi}\frac{\partial\theta}{\partial\lambda}\right)\left(\frac{1}{a}\frac{\partial\theta}{\partial\phi}\right)\times\left(\frac{1}{a\cos\phi}\frac{\partial v}{\partial\lambda}+\frac{1}{a}\frac{\partial u}{\partial\phi}+\frac{u\tan\phi}{a}\right). \quad (1)$$

Here, θ is the potential temperature, u and v are the zonal and meridional winds, respectively, and a, λ and ϕ are the radius of the Earth, longitude and latitude, respectively. Charron and Manzini (2002) showed that the FF calculated using relatively low-resolution data at a single height in the troposphere represents actual frontal region reasonably well. The height of FF calculation was chosen as ~600 hPa in Charron and Manzini, given that GWs emerge somewhat above the actual low-level fronts near ~800 hPa. Following Charron and Manzini (2002), the FF has been calculated at 600 hPa in some previous studies, such as Richter et al. (2010), Choi et al. (2018), and the current study. Through the thermal wind relationship (Holton 1992), fronts and jets are strongly related with each other, and large variations in the meteorological conditions, including GWs considered in the present study, exist across the front/jet systems.

2.2 Residual of Nonlinear Balance Equation (RNBE)

In the previous studies, the RNBE was formulated in Cartesian coordinates (e.g., Moore and Abeling 1988: Zhang et al. 2001) and used in regional areas. In the present study, we first derive the RNBE in spherical-p coordinates. A brief description of the derivation of the RNBE is given here. Using the zonal and meridional momentum equations in spherical coordinates (Holton 1992), the divergence equation can be obtained:

$$\frac{\partial D}{\partial t}+\vec{V}\cdot\vec{\nabla}D+\omega\frac{\partial D}{\partial p}=2J(u,v) +f\varsigma-\nabla^2\Phi-\beta u-D^2-\frac{\partial\vec{V}}{\partial p}\cdot\vec{\nabla}\omega +X, \quad (2)$$

where D is the divergence in the spherical coordinates given by:

$$D=\vec{\nabla}\cdot\vec{V}=\frac{1}{a\cos\phi}\frac{\partial u}{\partial\lambda}+\frac{1}{a\cos\phi}\frac{\partial}{\partial\phi}(v\cos\phi). \quad (3)$$

In (2) and (3), $\vec{V}$ is the horizontal wind vector, ω is vertical velocity in p-coordinate $\left(\omega\equiv\frac{Dp}{Dt}\right)$, $J(u,v)$ denotes the Jacobian, $f(=2\Omega\sin\phi$, where Ω is angular speed of rotation of the earth) and ς are the Coriolis parameter and vertical component of relative vorticity, respectively, Φ is the geopotential, $\beta(=2\Omega\cos\phi/a)$ is the latitudinal derivative of f, and X is the curvature term, which is expressed in the spherical-p coordinates as below:

$$X=-\frac{1}{a^2\cos\phi}\frac{\partial}{\partial\phi}\left[\left(u^2+v^2\right)\sin\phi\right]. \quad (4)$$

If large-scale flow is balanced, the right side of (2) should be zero, and thus the terms on the right-hand side of (2) represent the degree of imbalance from the nonlinear balance flow. Therefore, the RNBE in spherical coordinates can be written as:

$$RNBE\equiv 2J(u,v)+f\varsigma-\nabla^2\Phi-\beta u-D^2-\frac{\partial\vec{V}}{\partial p}\cdot\vec{\nabla}\omega+X. \quad (5)$$

The terms in (5) are the same as those derived in the Cartesian coordinates by Moore and Abeling (1988) and Zhang et al. (2001), except that the curvature term is included in the current study. In (5), the first four terms on the right-hand side are most dominant, which have been used mostly in the previous studies (e.g., Sato and Yoshiki 2008; Yoo et al. 2018), while the fifth and sixth terms are relatively small. We call the sum of the first four terms on the right-hand side as the major term, the sum of the fifth and sixth terms as the minor term, and the last term as the curvature term in Fig. 5. Although the RNBE can be evaluated at any altitudes, including stratosphere (e.g., Sato and Yoshiki 2008; Yoo et al. 2018), previous studies associated with upper-level jets in the troposphere selected height range from 350 hPa (e.g., Zhang 2004) to 200 hPa (e.g., Ki and Chun 2011; Song et al. 2017). Following Zhang (2004), we calculate RNBE at 350 hPa in the present study.

3 Spatiotemporal Variations in the FF and RNBE

3.1 Data

Spatiotemporal variations in the FF and RNBE are examined using the Modern-Era Retrospective analysis for Research and Applications (MERRA: Rienecker and Coauthors 2011) and the Interim European Centre for Medium-Range Weather Forecasts (ECMWF) Re-Analysis (ERA-Interim: Dee and Coauthors 2011) for 32 years from January 1, 1980 to December 31, 2011. The MERRA data have a horizontal resolution of 1.25° × 1.25° (latitude x longitude) from the surface to 0.1 hPa at 42 levels every 3 h, while the ERA-Interim data have horizontal resolution of 1.5° × 1.5° from the surface to 1 hPa at 37 levels every 6 h. Horizontal and vertical winds, temperature, and geopotential fields are used to calculate the FF and RNBE. In the present study, we used 6-hly MERRA data to directly compare with the results from the ERA-Interim data. Following Charron and Manzini (2002), the FF and RNBE are not considered poleward of 75°N and 75°S, at which the high sensitivity to anomalies in the data assimilation process can render the analysis data untrustworthy.

3.2 Frontogenesis Function (FF)

Figure 1 shows the horizontal distribution of FF at 0000 UTC 16 January 2011 (upper) and 0000 UTC 16 July 2011 (lower) at 600 hPa from the MERRA (left) and ERA-Interim (right) data sets. It shows that the FF is large poleward of approximately 30° in both the winter and summer hemispheres, with larger values in the winter hemisphere than in the summer hemisphere. Although both positive and negative FFs appear

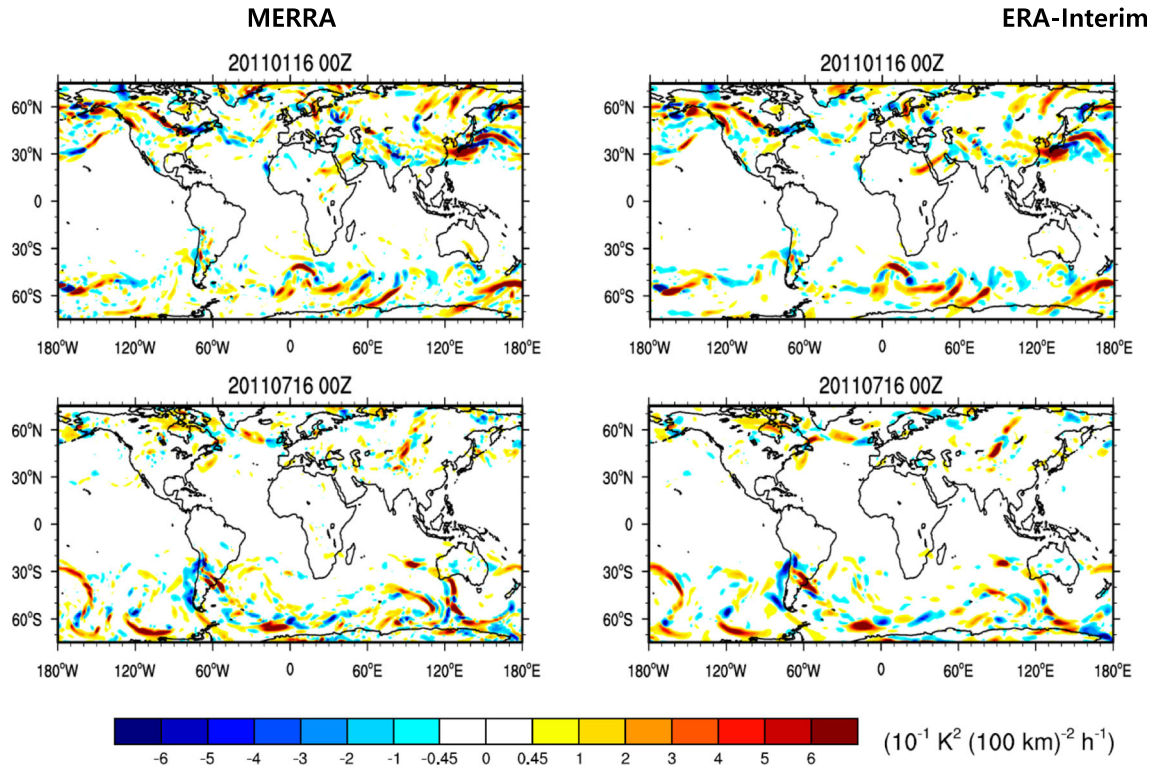

Fig. 1 Longitude-latitude cross-sections of the FF at 600 hPa, 0000 UTC 16 Jan 2011 (upper) and 0000 UTC 16 July 2011 (lower) calculated using MERRA (left) and ERA-Interim (right) data

at the instant time, positive values are dominant with wavy structure at higher latitudes, which is likely related to fronts and storm tracks associated with synoptic features. Note that positive FF implies an increase of horizontal temperature gradient, which is a real meaning of *frontogenesis*, while negative FF implies a decay of a front, called *frontolysis* (AMS 2000). Therefore, only positive value of FF is meaningful to represent the frontogenesis function, which is used exclusively in the correlation coefficient calculation in section 5. The results from the two different reanalysis data sets are generally similar, although magnitudes are slightly larger and smaller-scale features are more evident from MERRA data, due likely to better horizontal resolution compared to the ERA-Interim data. To calculate the FF at 600 hPa in regions with mountains higher than 600 hPa, variables are interpolated from MERRA data, following the method used in WACCM (Richter et al. 2010), while the ERA-Interim reanalysis data used in the present study are those provided after interpolation. In Fig. 1, magnitudes larger than 0.045 KP^2P (100 km)$P^{-1}P$ $hP^{-1}P$ are colored, and this value was used as a threshold to turn on the frontal GWD scheme in WACCM by Richter et al. (2010) and a GCM by Choi et al. (2018). Although slightly larger thresholds have been used in some previous studies [e.g., 0.07 KP^2P (100 km)$P^{-1}P$ $hP^{-1}P$ in Griffiths and Reeder 1996; 0.1 KP^2P (100 km)$P^{-1}P$ $hP^{-1}P$ in Charron and Manzini 2002], we found that the current threshold is a reasonably good indicator of frontal GWs when we examine the correlation with the GWMF obtained from high-resolution ECMWF analysis data, which will be discussed in section 5. In addition, the regions with a FF larger than the current threshold are successfully separated from the regions of major convection activities between 30°S and 30°N. Note that the magnitude of the FF considered in the present study is much smaller in the tropical regions than in the mid-to-high latitudes, likely because the large-scale horizontal temperature gradient (baroclinicity) and horizontal winds and their horizontal gradients are smaller in the tropical region. In addition, diabatic heating effects, which should be larger in the tropical region associated with convective clouds, are ignored in Eq. (1).

Figure 2 shows 32-year mean seasonal climatology of the FF at 600 hPa in December–January-February (DJF), March–April-May (MAM), June–July-August (JJA), and September–October-November (SON) calculated using the MERRA

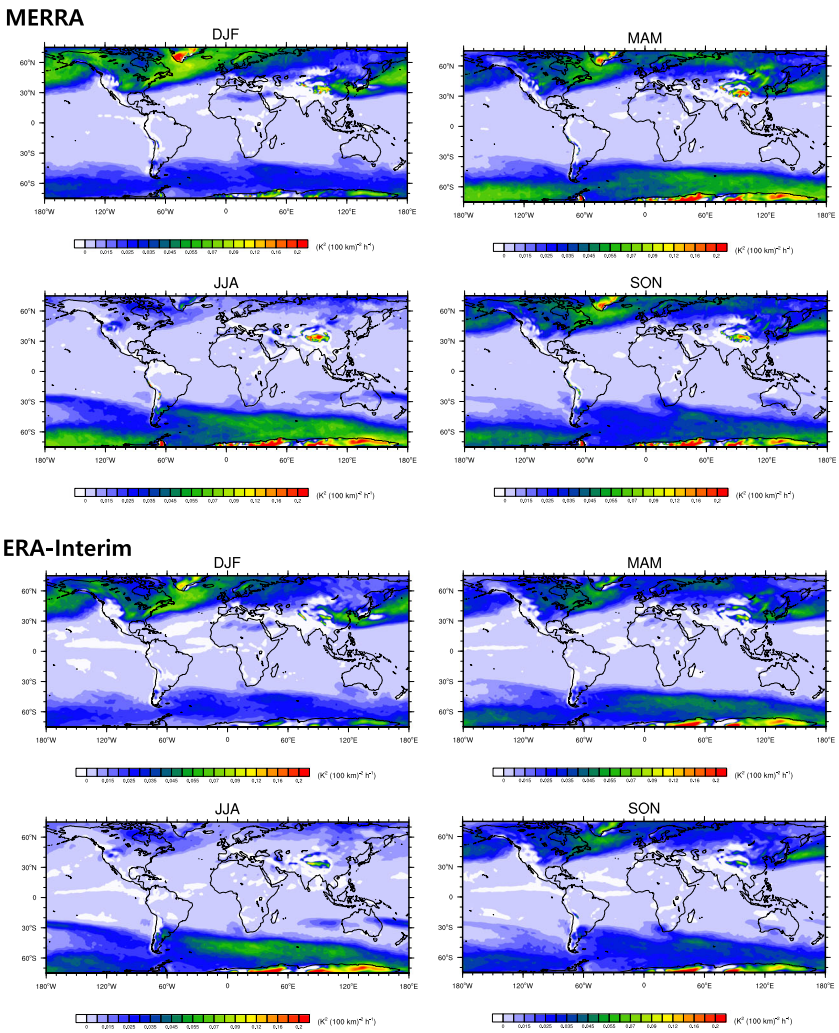

Fig. 2 Seasonal climatology of the 32-year mean of the FF at 600 hPa in December–January-February (DJF), March–April-May (MAM), June–July-August (JJA), and September–October-November (SON) calculated using MERRA (upper) and ERA-Interim (lower) data

(upper) and ERA-Interim (lower). Several interesting features can be found in this figure. First, there is a clear seasonal march in the FF in both hemispheres, which is the largest in the winter, decreasing in the spring, the smallest in the summer, and increasing in the fall. Second, in the NH, the FF is dominant in three regions, especially in wintertime; the North Atlantic region including Greenland, East Asia, and Pacific storm tracks extending to Alaska. The local maxima of the FF exist at the southern tip and east coast of Greenland. The southern tip of Greenland and its downstream are well-known areas of mountain waves and clear-air turbulence related to the breaking of the mountain waves (e.g., Sharman et al. 2012). Based on the high-resolution ECMWF data and back-trajectory analysis of GWs, Preusse et al. (2014) suggested the fronts as potential sources of stratospheric GWs in the North Atlantic region, which is consistent with the strong FF regions in the present study. The relatively large value of the FF in East Asia over Korea and Japan is located very near the center of the subtropical jet, which will be shown in Fig. 3, but its magnitude significantly decreases in JJA and SON. The region of the Pacific storm tracks is located downstream of the major subtropical jet, and the FF in this area is sustained in most seasons, except in JJA. There is a local maximum over the Tibetan Plateau (~90P°PE-100P°PE, 30P°PN), which is persistent for nearly all seasons with the strongest magnitude in JJA, likely due to elevated surface sensible heating and convective latent heating. The value of FF over the Tibetan Plateau is larger in the MERRA than ERA-Interim data (Fig. 2), likely related to the horizontal resolution.

Third, in the SH, large positive values are shown near the Antarctic Peninsula in most seasons except in the summer (DJF). The large amplitude of the GWMF in the SH high latitudes in July has been shown from satellite measurements by the Sounding of the Atmosphere using Broadband Emission Radiometry (SABER) instrument and the High Resolution Dynamics Limb Sounder (HIRDLS) in Jia et al. (2014), which suggested polar-night jets and topography as potential sources of GWs in these areas. The areas of large amplitude of GWMF in Jia et al. (2014) and the large FF in the SH high latitudes in Fig. 2 are generally matched, although a local maximum of the FF exists in the Antarctic Peninsula but a local maximum of the GWMF in Jia et al. (2014) exist along latitude bands near 40P°PS-60°S in the Southern Ocean. The large magnitude GWMF near 40P°PS-50°S in the Southern Ocean in winter is also related to the convective GWs shown recently from Kang and Chun (2017). It is interesting that the FF in the Antarctic Peninsula is larger from ERA-interim than from MERRA data in most seasons, except in DJF, regardless of relatively low horizontal resolution of ERA-Interim. This is likely related to differences in latitudinal coverage and the interpolation method near the plateau between the two data sets. The temporal variations in the FF averaged over major locations near Greenland, East Asia, the southern tip of the

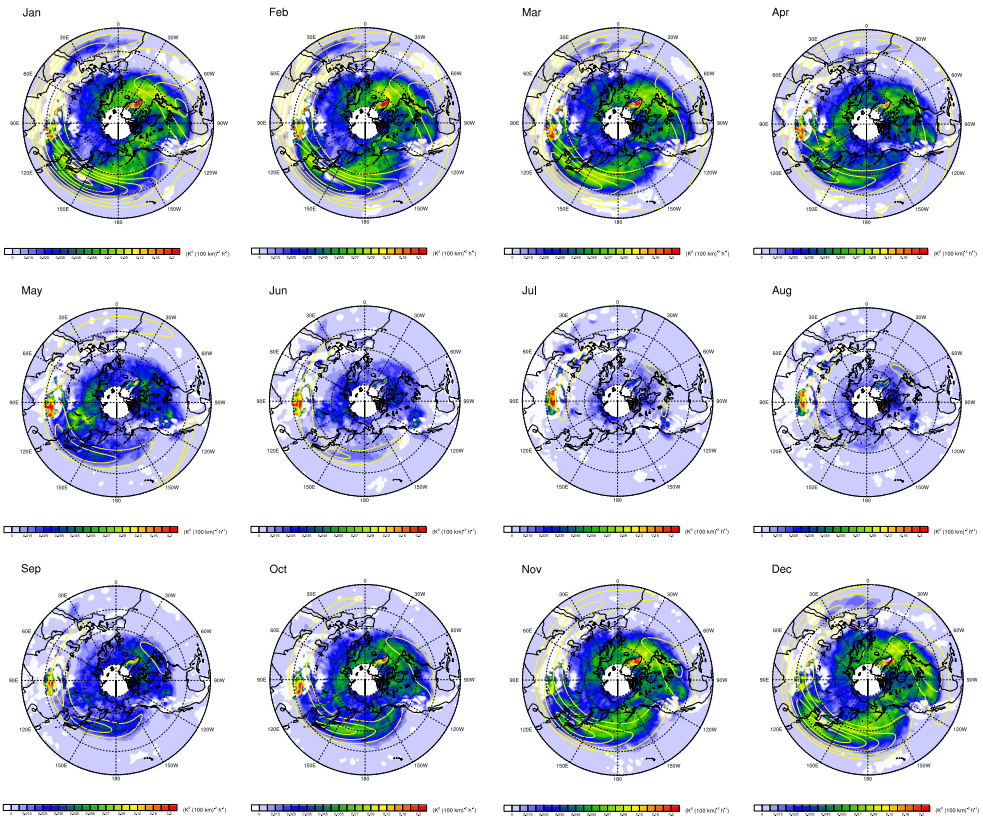

Fig. 3 Polar stereo-projection maps of the FF (shading) at 600 hPa superimposed on the monthly mean zonal wind at 200 hPa (yellow contour) in the NH averaged over 1980–2011 (32 years) calculated using MERRA data. The contour intervals of the zonal wind are 10 m $sP^{-1}P$ starting from 25 m $sP^{-1}P$. Latitude circles are drawn every 15° and meridians every 30°, with the Greenwich meridian pointing upward to the top of the figure

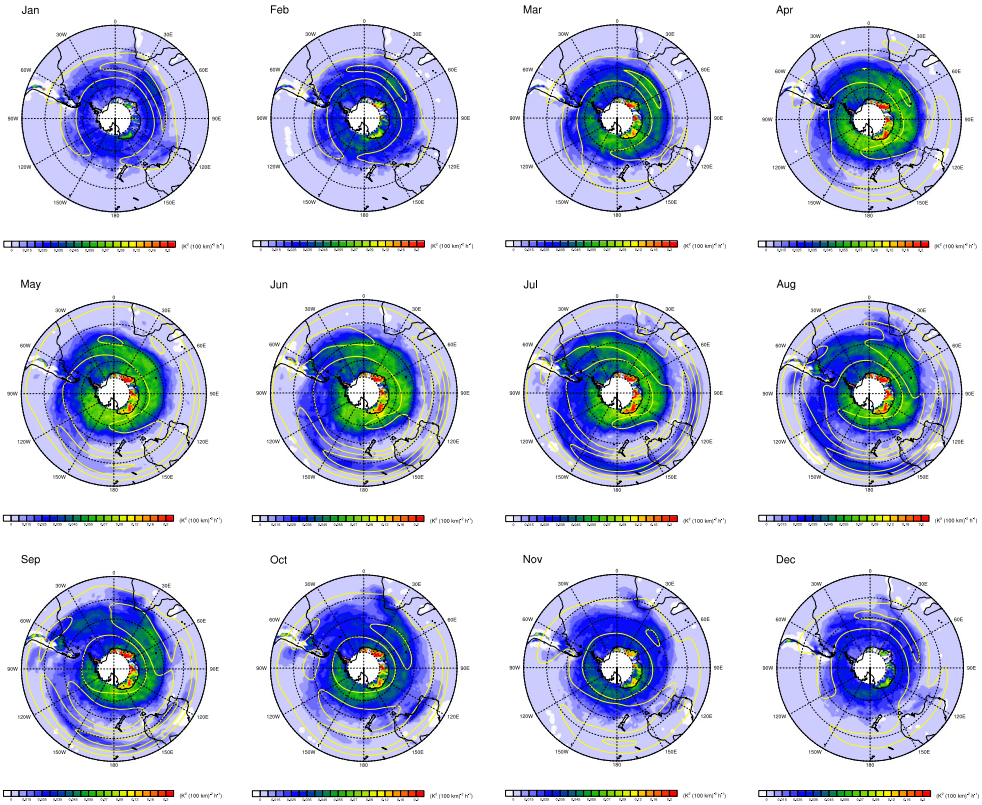

Fig. 4 The same as in Fig. 3, except in the SH

Andes Mountains, and the Antarctic Peninsula reveal (not shown) a clear seasonal cycle with a maximum in the winter and a minimum in the summer, without significant interannual variability during the 32-year period.

To understand the correlation between the FF and upper tropospheric jets, we show in Figs. 3 and 4 the 32-year mean values of the FF at 600 hPa for each month, along with the 32-year mean values of the zonal wind at 200 hPa in the NH (Fig. 3) and SH (Fig. 4) calculated using MERRA data. Because of the generally similar pattern in the FF, as shown in Figs. 1 and 2, and the location of the jet at 200 hPa (not shown), the results calculated using ERA-Interim data are not included in these figures. Seasonal changes in the FF and the correlation between the FF and the subtropical jet are clearly observed here. The maximum FF near Greenland and the Norwegian Sea is sustained for approximately 7 months from October to April, and it is located on the northeast of the 200 hPa jet, which exists to the east of North America, at a significant distance. The regions of the large FF near Greenland and the Norwegian Sea are nearly stationary during October to April, although the magnitude changes in the FF follow the strength of the jet. Contrarily, the secondary peak of the FF in East Asia, as shown in Fig. 2, is located near the jet core, following the movement of jet core. In summer months, FF is very weak, except a local maximum over the Tibetan Plateau, and the areas of relatively large FF (with blue color) locate poleward of the 200 hPa jet that moves northward to 45°N-60°N. The FF in the region from the Pacific storm tracks to Alaska on the downstream of the primary subtropical jet is sustained for approximately 5 months from November to March. In the SH (Fig. 4), a large FF exists in the Antarctic Peninsula and Southern Ocean along approximately 60°S latitude bands in winter months, especially in the eastern hemisphere. Although large FFs exist near the center of the jet in the summer and fall months (February–May) in the eastern hemisphere, the FF is not well correlated with the jet at 200 hPa in winter months, which is different from the NH.

3.3 Residual of Nonlinear Balance Equation (RNBE)

Figure 5 shows global distribution of the major, minor, curvature, and total terms of the RNBE at 350 hPa at instant time (0000 UTC January 16, 2011) calculated using MERRA (left) and ERA-Interim (right) data. The RNBE has much smaller horizontal scale than the FF with consecutive positive and negative values. This is different from the FF (Fig. 1), which has a longer horizontal scale with dominant positive values. The careful examination of each terms included in the RNBE formulation (5) reveals that the localized features shown in Figure 5 are mainly due to the third term on the right-hand side of (5), $\nabla^2\Phi$, which is the only term with the second-order derivative among all terms included in the FF and RNBE formulations. Although large values exist poleward of 30° in both the NH and SH, the RNBE is distributed widely in latitudes, including in some regions in the subtropics and tropics, such as the South China Sea, northern Australia, southern tip of Andes, the west coast of Mexico, and the African

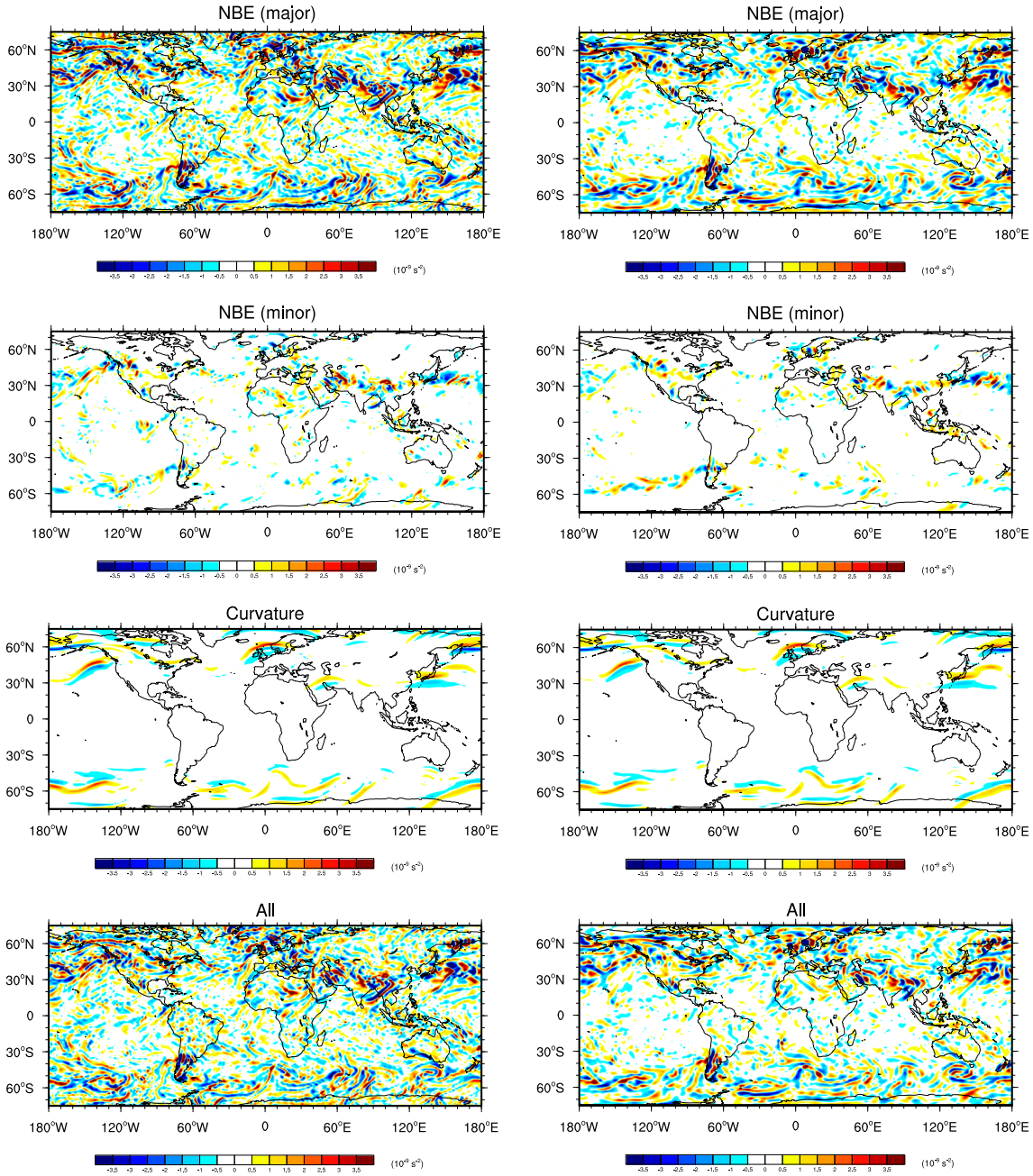

Fig. 5 Longitude-latitude cross-sections of major, minor, curvature, and total terms of RNBE at 350 hPa and 0000 UTC 16 January 2011 calculated using MERRA (left) and ERA-Interim (right) data

Continent. Both minor and curvature terms are non-negligible in some local regions, so that the RNBE including all terms in (5) is considered hereafter, unlike most previous studies that considered only the major term of the RNBE. The distribution and magnitude of the RNBE calculated using MERRA and ERA-Interim are generally similar to each other, although the similarity is relatively weak compared with the FF (Fig. 1), likely due to that the higher-order derivative term ($\nabla^2\Phi$) in RNBE makes the result sensitive to the horizontal resolution.

Figure 6 shows the 32-year average of seasonal change in the RNBE calculated using MERRA. There are several regions of local maxima near Greenland, western North America, East Asia, the Andes Mountains, and the Antarctic Peninsula, with a clear seasonal march; maximum in wintertime and minimum in summertime. However, in some regions in the SH, such as the tip of the Andes and the Antarctic Peninsula, RNBE is large for most seasons, except in the summer (DJF). The large RNBE in western North America, the Andes Mountains, and the Antarctic Peninsula are not matched with regions of a strong FF. The flow near steep mountains, for instant near the Andes Mountains in winter where strong westerlies are impinging on steep grid-resolved

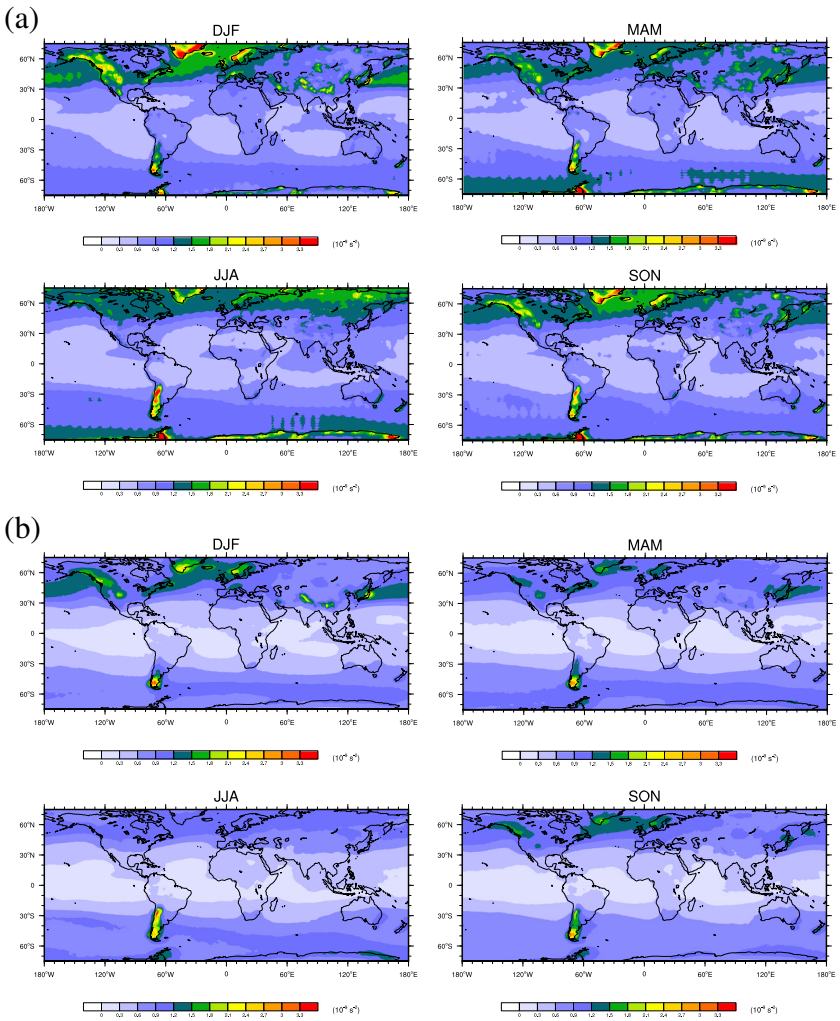

Fig. 6 Seasonal changes in the absolute value of RNBE at 350 hPa averaged over 1980–2011 (32 years) calculated using (a) MERRA and (b) ERA-Interim data

mountains elongated in north-south direction, can produce divergence and RNBE in addition to near the jet stream, as also shown in Song et al. (2017). Nevertheless, each term included in the RNBE is not found to be particularly strong near other major mountains such as Himalaya. When a RNBE-based GWD parameterization is implemented to WACCM (Part II paper) under the existing orographic GWD parameterization, it may need to separate orographic effect from the RNBE diagnostics. One feasible way may be to calculate the RNBE using variables at each model grid after a low-pass filtering, such as done by Sato and Yoshiki (2008). We found (not shown) that local peaks near steep mountains disappear by the low-pass filtering process. However, applying the low-pass filtering to the GWD parameterization leads to some complexities including additional computing time. There are several other practical issues in the implementation of a RNBE-based GW parameterization to GCM, which will be discussed in Part II. The monthly mean time series of the RNBE averaged over the five selected regions of the large RNBE (near Greenland, western North America, East Asia, the Andes Mountains, and the Antarctic Peninsula) revealed (not shown) a clear annual cycle without significant interannual variations, as also found for the FF.

To understand the correlation between the RNBE and upper tropospheric jets, we show in Figs. 7 and 8 the 32-year mean values of the RNBE at 350 hPa for each month along with the 32-year mean values of the zonal wind at 200 hPa in the NH (Fig. 7) and the SH (Fig. 8) that are calculated using MERRA. The locations of large RNBE relative to the 200 hPa jet are generally similar to those for the FF, except that a large RNBE exists on the northeast of the cores of the major jets in the NH wintertime (Fig. 7) and a large RNBE is sustained along the Andes Mountains (Fig. 8).

4 GWMF Estimated from High-Resolution Global Analysis Data

To examine whether the two diagnostics represent GWs associated with jet/frontal systems reasonably well, we estimated the GWMF from high-resolution ECMWF analysis data (Untch et al. 2006) with a horizontal resolution of 0.25°.

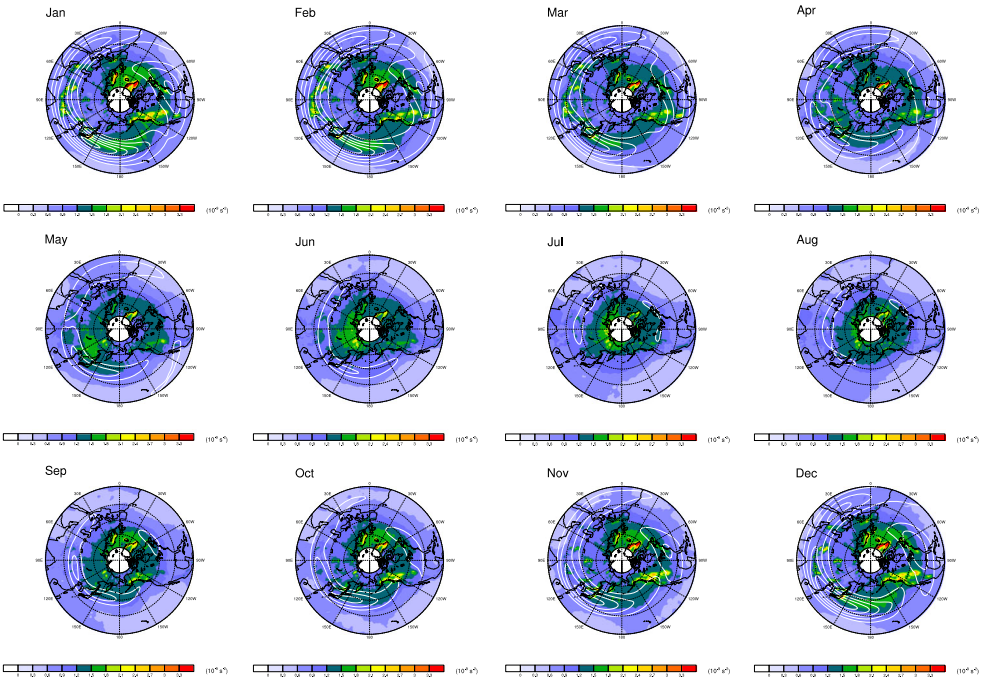

Fig. 7 Polar stereo-projection maps of RNBE (shading) at 350 hPa superimposed on the monthly mean zonal wind at 200 hPa (white contour) in the NH averaged over 1980–2011 (32 years) calculated using MERRA data. The contour interval of the zonal wind is 10 m $sP^{-1}P$ starting from 25 m $sP^{-1}P$. Latitude circles are drawn every 15° and meridians of every 30°, with the Greenwich meridian pointing upward to the top of the figure

Considering that horizontal wavelengths longer than approximately 150–200 km (approximately 6–8Δx, where Δx is the horizontal grid spacing) are resolvable with that resolution (Lane and Knievel 2005), the ECMWF analysis data are reasonably good to study GWs associated with jet/frontal systems. Note, however, that the horizontal and vertical resolutions of the ECMWF data are not sufficient to resolve the *full* spectrum of GWs associated with jet/frontal systems. In particular, the vertical resolution of the model to produce the ECMWF analysis data is not sufficient to resolve the full spectrum of GWs in the stratosphere, which is about 500 m in the lower stratosphere and more than 2 km in the upper stratosphere (Persson and Grazzini 2005). A recent work by jet-frontal GWs observed from the Esrange MST radar (67.88°N, 21.10°E) by Réchou et al. (2015) demonstrated that the momentum flux carried by the GWs with vertical wavelengths of less than 1 km is about one order of magnitude larger than that by the GWs with vertical wavelengths longer

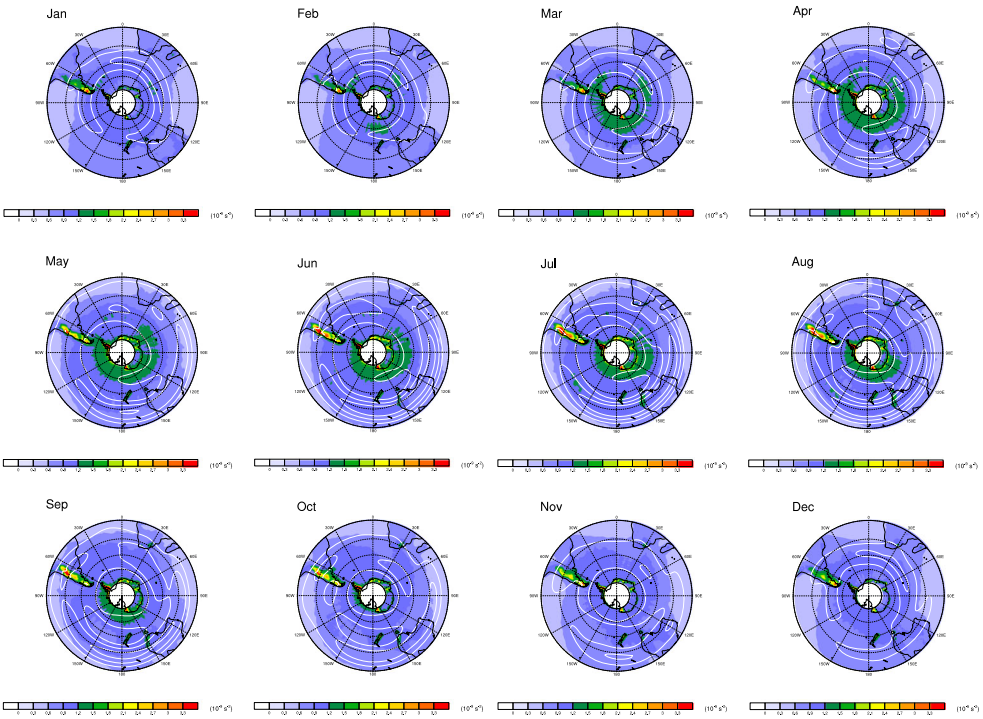

Fig. 8 The same as in Fig. 7, except in the SH

than 1 km. Due to a limitation of data availability, we can use 6-h data over two months in January and July of 2007 at three selected levels in the upper troposphere (300 hPa), lower stratosphere (70 hPa), and upper stratosphere (5 hPa). The zonal ($\rho_0\overline{u'w'}$) and meridional ($\rho_0\overline{v'w'}$) momentum fluxes of gravity waves are obtained, where ρ_0 is the density of standard atmosphere, and u', v', and w' are the zonal, meridional, and vertical wind perturbations, respectively. The perturbation is obtained after subtracting the mean value (denoted by the over-bar) that is defined as the 21 × 21 points horizontal running average of the variables. This method was used in previous studies by Kim and Chun (2010) and Kim et al. (2012) using the high-resolution ECMWF analysis data.

Figure 9 shows the monthly mean zonal momentum flux in January (left) and July (right) of 2007. The zonal mean values of the momentum flux and zonal wind are shown on the right of each plot. In the upper troposphere (300 hPa), both negative and positive momentum fluxes exist, although negative momentum flux is dominant in the extratropics, especially in the winter hemisphere. The magnitude of the negative momentum in the mid-latitudes of the winter hemisphere is larger in the SH than in the NH. The positive momentum flux is dominant in the intertropical convergence zone (ITCZ), where the zonal-mean zonal wind is near zero. In the lower stratosphere (70 hPa), a negative momentum flex in the winter extratropics and a positive momentum flux in the summer subtropics are the general features in both hemispheres. This is mainly due to filtering by the background wind, which changes from westerly to easterly between the upper troposphere and lower stratosphere. In the upper stratosphere (5 hPa), areas of negative momentum flux are squeezed further poleward, as the positive zonal-mean zonal wind shift poleward. The positive momentum in the summer subtropics is the secondary peak and is smaller in the SH than in the NH. Because of the wave filtering by background wind and the reduction in density with height, the magnitude of the momentum flux significantly decreases with height. The potential sources of the GWs in the winter hemisphere mid-to-high latitudes are mountains and jet/frontal systems, whereas the primary source in the summer subtropics is convective clouds.

The meridional momentum flux (Fig. 10) at 300 hPa is mostly positive in the NH and negative in the SH without seasonal change, which is quite different from the zonal momentum flux. This implies that GWs propagate either upward and poleward or downward and equatorward. If the sources of GWs are located in the troposphere, including the upper troposphere near 300 hPa, this result indicates the dominance of upward and poleward wave propagation. The local maxima exist near 35° in the winter hemisphere and 45° in the summer hemisphere. Although the sign of the zonal-mean meridional wind is opposite to that of the meridional momentum flux in mid-to-high latitudes, it is not as clear as in the zonal momentum flux, especially near 30°S-30°N. At 70 hPa, the momentum flux significantly decreases, and it is mainly positive in the NH mid-latitudes and negative in the SH mid-latitudes, with local maxima near the tip of the Andes and the Antarctic Peninsula, under nearly zero zonal-mean meridional wind for all latitudes. This feature

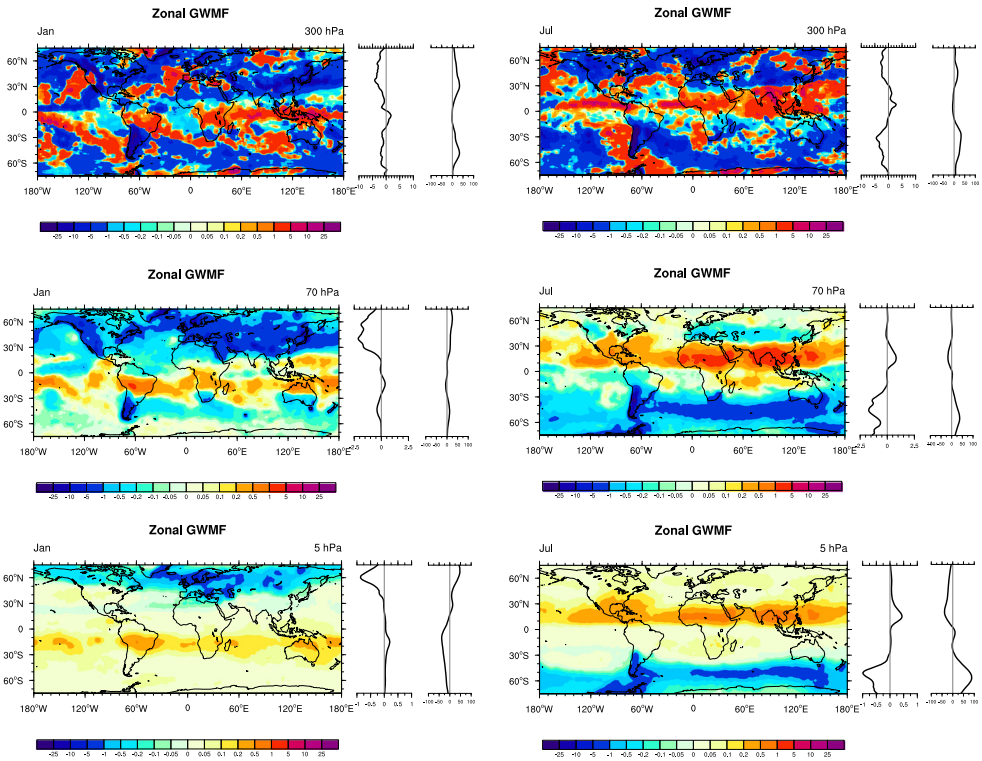

Fig. 9 Monthly mean of the zonal GWMF estimated from high-resolution ECMWF analysis data at three selected levels in January (left) and July (right) of 2007. The two profiles on the right-hand side of each longitude-latitude cross-section denote the zonal-mean GWMF and the zonal-mean zonal wind, respectively

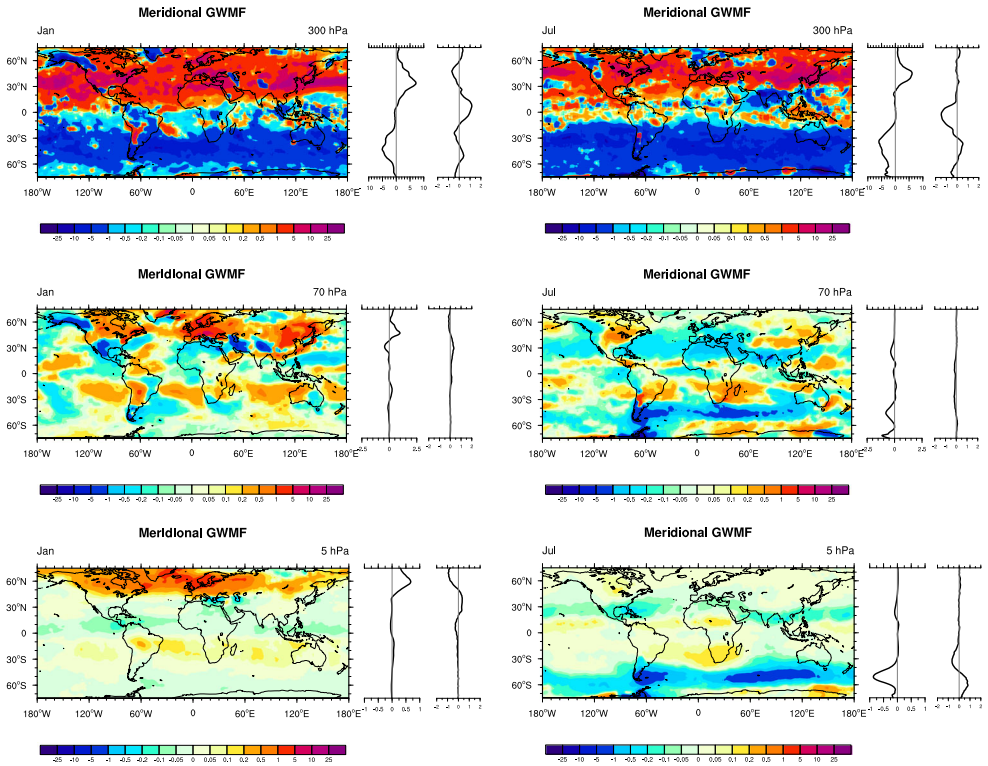

Fig. 10 The same as in Fig. 9, except for the meridional momentum flux

remains up to 5 hPa, at which only positive (negative) momentum in the NH (SH) high latitudes is noticeable.

The sources of GWs revealed in the high-resolution ECMWF data have been recently discussed by Preusse et al. (2014) and utilize backward ray-tracing calculations of GWs. They showed that strong GWs in northern Norway are related to a frontal system and that strong GWs in the Antarctic winter polar vortex originate from jet instabilities around the tropopause or in the lower stratosphere. They also showed that almost all rays pass above a convective system in the upper troposphere and lower stratosphere. In the present study, we emphasize the feasibility of the two diagnostics (FF and RNBE) of GWs associated with jet/frontal systems, and a detailed analysis of the potential sources of GWs revealed in the high-resolution ECMWF data is beyond the scope of the current study, although it remains a future research topic.

The GWMF estimated from the high-resolution ECMWF data is compared with satellite observations from HIRDLS (Ern et al. 2011). Note that GWs observed from HIRDLS are those with horizontal wavelengths longer than 100–200 km and vertical wavelengths longer than about 2 km (Ern et al. 2011). Figure 11 shows the absolute value of the GWMF estimated from the high-resolution ECMWF analysis data at 5 hPa (left) and that from HIRDLS at z = 35 km, which is close to 5 hPa, in January (upper) and July (lower) of 2007. The absolute GWMF of the ECMWF data is obtained by taking the square root of the zonal and meridional momentum fluxes shown in Figs. 9 and 10. The general features of the two results are similar, except that the GWMF from ECMWF in the high latitudes of the SH is 2–3 times smaller than that from HIRDLS, and the secondary maximum in the summer hemisphere subtropics is also much smaller both in January and July. Nevertheless, the pattern correlation between the two datasets in January and July of 2007 is as high as 0.86 (0.85) and 0.90 (0.88), respectively, in the NH (SH). Note that only the monthly mean GWMF is available from HIRDLS, while a 6-hour GWMF from the high-resolution ECMWF analysis data is available only for two months (January and July of 2007). Because of this limitation in data availability, a pattern correlation calculation in the monthly mean absolute GWMF in January and July of 2007 is performed. Recently, Alexander (2015) showed that the GWMF from the HIRDLS measurements based on 2-dimensional properties of GWs may be significantly underestimated. Considering this possibility, the 2–3 times smaller magnitude of the GWMF from the ECMWF analysis compared with HIRDLS shown in Fig. 11 implies that current GCMs with high horizontal resolution (approximately 0.25° × 0.25°), such as the ECMWF model and recently developed WACCM (Liu et al. 2014), may significantly underestimate the GWMF. This result suggests that further improvement in the representation of GWs in GCMs is requested in the stratosphere, presumably by improving physical processes that control the spatiotemporal variations in GW sources in the troposphere and by increasing the vertical resolution, which allows better representation of propagation and dissipation processes of GWs (Choi and Chun 2008; Richter et al. 2014).

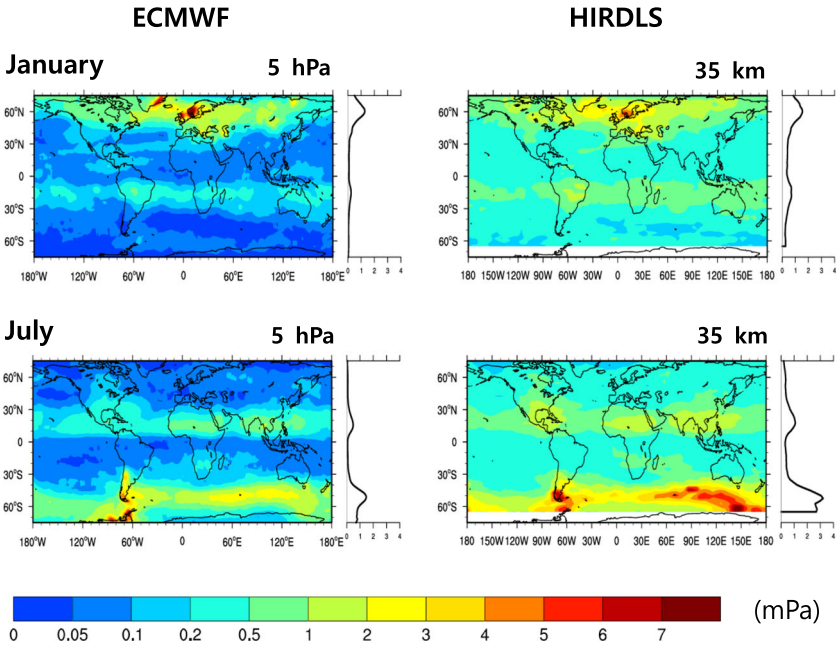

Fig. 11 Absolute GWMF estimated from high-resolution ECMWF analysis data at 5 hPa (left) and HIRDLS observations at z = 35 km (right) in January (upper) and July (lower) of 2007. The profile on the right-hand side of each latitude-longitude cross-section denotes the zonal mean value

5 Correlation between GWMF and Diagnostics (FF and RNBE)

To examine whether the FF and RNBE are the feasible diagnostics of GWs associated with jet/front systems, we calculated the correlation coefficient between the 6-hourly GWMF estimated from the ECMWF analysis data, which is shown in Figs. 9 and 10, and the FF and RNBE calculated using 6-hourly MERRA and ERA-Interim data, as shown in Figs. 1, 2, 3, 4, 5, 6, 7, and 8. Here, a positive FF at 600 hPa and an absolute RNBE at 350 hPa every 6 h are used for the calculation of the correlation, after which the GWMF from the ECMWF analysis data with 0.25° × 0.25° horizontal resolution is matched with the MERRA and ERA-Interim grid spacing. Figure 12 shows the correlation coefficient between the zonal GWMF at each of 300 hPa, 70 hPa, and 5 hPa and the FF at 600 hPa, which is calculated using MERRA (left) and ERA-Interim (right) in January (Fig. 12a) and July (Fig. 12b). Values that satisfy a 90% confidence level are colored. Several interesting features are shown in Fig. 12. First, at 300 hPa, the correlation is stronger in the mid-to-high latitudes in both hemispheres with some local peaks, such as the southern tip of the Andes, North Africa and southern Europe, North America, and southern Australia. Second, the correlation generally decreases with height, which is somewhat expected because several processes, such as the filtering, horizontal propagation, and time lag, between 600 hPa, where FF is evaluated, and the heights (300, 70, and 5 hPa) where GWMFs are evaluated cannot be considered in this correlation calculation. However, there are several local points where a strong correlation is sustained up to the lower stratosphere (70 hPa), such as the southern tip of the Andes, North Africa and southern Europe, North America, and southern Australia. These features are generally similar in July (Fig. 12b), although notably strong values appear from the South China Sea to eastern Japan at 300 hPa, presumably related to frontal activities in the summer monsoon season. Negative correlations appear in summer hemispheres of some local regions at 70 hPa and of most regions at 5 hPa. This is likely due to changes in the background wind in summertime from westerlies in the upper troposphere to easterlies in the stratosphere, which leads to significant filtering of negative GWMF in the stratosphere. The correlation between GWMF and the FF calculated using the two reanalysis datasets is very similar to each other, although the correlation coefficient is slightly larger when the FF is calculated using the ERA-Interim data, likely because the GWMF is estimated using the high-resolution ECMWF analysis data, which are produced using the same basis model of ERA-Interim.

Figure 13 is the same as Fig. 12 except for the correlation between the zonal GWMF and the RNBE. As in Fig. 12, strong correlations between the zonal GWMF and the RNBE exist in mid-to-high latitudes in both hemispheres at 300 hPa, with values much larger than those between the GWMF and the FF. This is somewhat expected, given that RNBE is calculated at 350 hPa, very near 300 hPa, where the small-scale resolved unbalanced structures are spanning around those levels and the filtering, horizontal propagation, and time lag between the level of diagnostics (350 hPa) and GWs (300 hPa) are limited, compared with the FF, which is calculated at 600 hPa. The local maximum points are generally similar to those in Fig. 12, except that values in the south of Greenland and western North America in January and the southern tip of Africa, the Andes Mountains, and the Antarctic

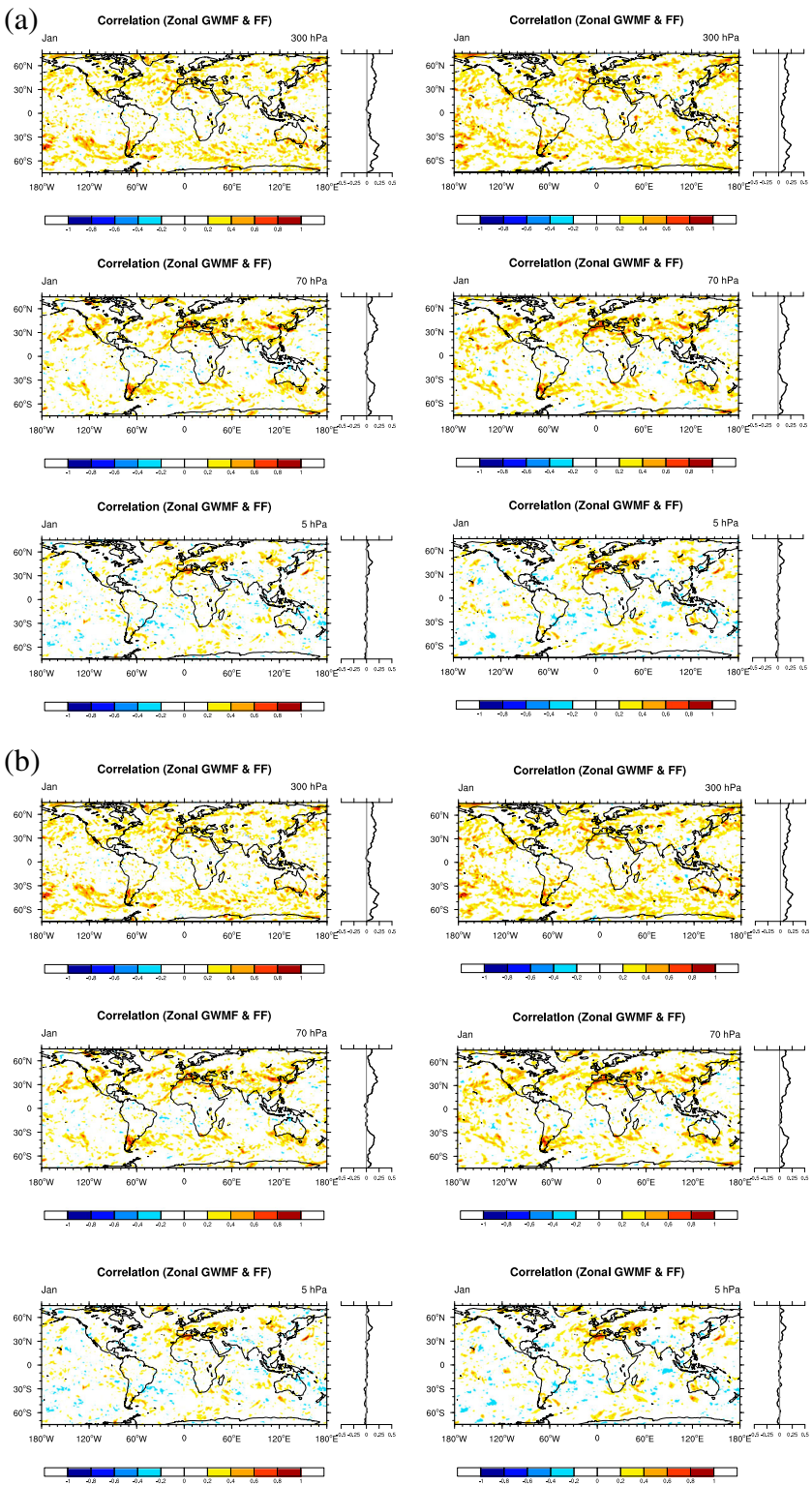

Fig. 12 Correlation between the FF, which is calculated using MERRA (left) and ERA-Interim (right) data, and zonal GWMF estimated from high-resolution ECMWF analysis data in (**a**) January and (**b**) July of 2007. The profile on the right-hand side of each latitude-longitude cross-section denotes the zonal mean correlation

Peninsula in July are much larger than those between the GWMF and the FF. Strong correlations in the aforementioned local regions are sustained up to 70 hPa, and even at 5 hPa, exclusively in the winter hemisphere. In particular, values larger than 0.8 exists at 5 hPa in southwest Greenland in January and in the southern Andes in July. As in Fig. 12, a negative correlation appears in the summer stratosphere, mostly at 5 hPa. As in the correlation between the GWMF and FF (Fig. 12), the results using the two reanalysis datasets are similar to each other, including local maxima, and correlation coefficients are slightly larger when the RNBE is calculated using the ERA-Interim data than the MERRA data.

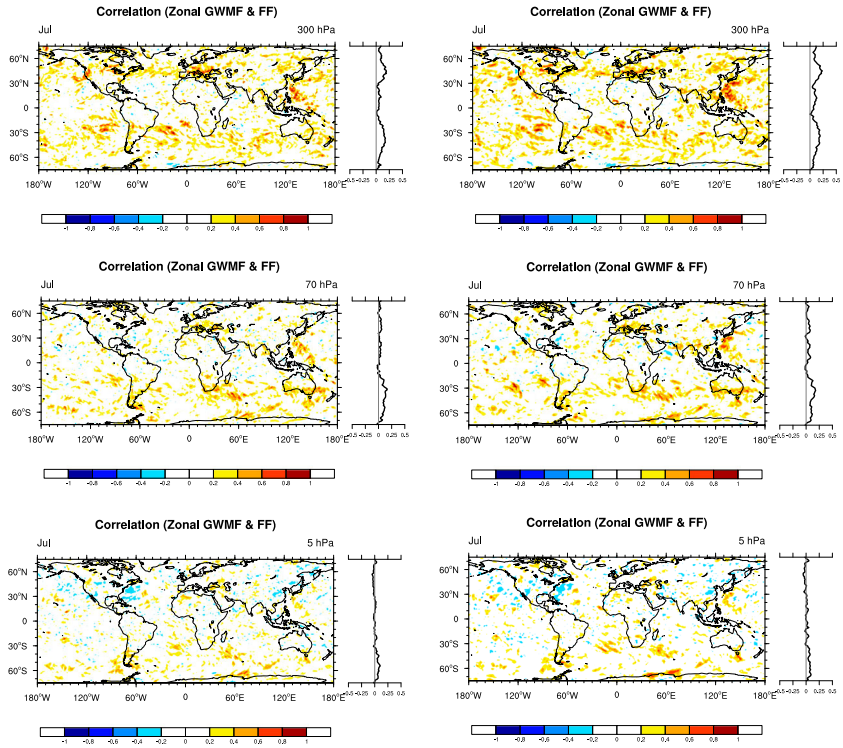

Fig. 12 (continued)

The correlations between the meridional GWMF and the two diagnostics are shown in Fig. 14 for July. For the FF (Fig. 14a), correlations with the meridional GWMF are generally similar to those with the zonal GWMF (Fig. 12b), although with smaller values of local maxima and minima. In particular, the strong negative correlation at 5 hPa near the East Coast of North America shown in Fig. 12b is significantly reduced. The correlation between the RNBE and the meridional GWMF (Fig. 14b) is clearly different from that between the RNBE and the zonal GWMF. First, the strong correlation along the Andes Mountains from 30°S-60°S at 300 hPa shown in Fig. 13b no longer appears, while stronger correlations appear to the west and east of southern Africa near 30°S. Consequently, the zonally averaged correlation shown in Fig. 14b is similar to Fig. 13b. The regions of local maxima at 70 and 5 hPa are generally consistent with those shown in Fig. 12b, with much smaller values according to the reduced magnitude at 300 hPa. The results in January (not shown) are generally consistent with Fig. 14, considering the seasonal changes in each hemisphere.

6 Summary and Conclusions

Jet/front systems are one of the major sources of atmospheric gravity waves (GWs) that contribute significantly to global circulation in the middle atmosphere. Based on the mesoscale simulation results (e.g., Wang and Zhang 2007; Kim et al. 2016), the dominant GWs associated with the jet/front systems have horizontal wavelengths of approximately 150 km, which are generated preferentially in the exit region of the upper-level jet stream, and they should be parameterized in GCMs. Nevertheless, there is no comprehensive parameterization of GWs associated with jet/front systems, with formulations of the GW momentum flux at the launch level considering the sources explicitly, due mainly to uncertainties in their generational mechanisms. However, some efforts have been made to include the frontal GWD parameterization scheme in GCMs (e.g., Charron and Manzini 2002; Richter et al. 2010; Choi et al. 2018), which used the FF calculated at GCM grids as a diagnostic of GW generation. This approach is still much better than the commonly used background GWD scheme that assigns an arbitrarily determined uniform GWMF at every model grid. Before a comprehensive parameterization scheme of GWs associated with jet/frontal systems is developed, the feasibility of the FF as a diagnostic of jet/frontal GWs and the possibility of using another diagnostic, the residual of nonlinear balance equation (RNBE) that has been used widely to represent GWs associated with the upper-tropospheric jet, should be examined.

In this study, we investigated the spatiotemporal variations in two diagnostics, the FF and RNBE, of atmospheric gravity waves associated with jet/frontal systems, using the two 32-year (1980–2011) global reanalysis data sets (MERRA and ERA-Interim). The fronts and jets are strongly correlated with each other in the large-scale flow through the thermal wind relationship. In the present study, the FF is calculated at

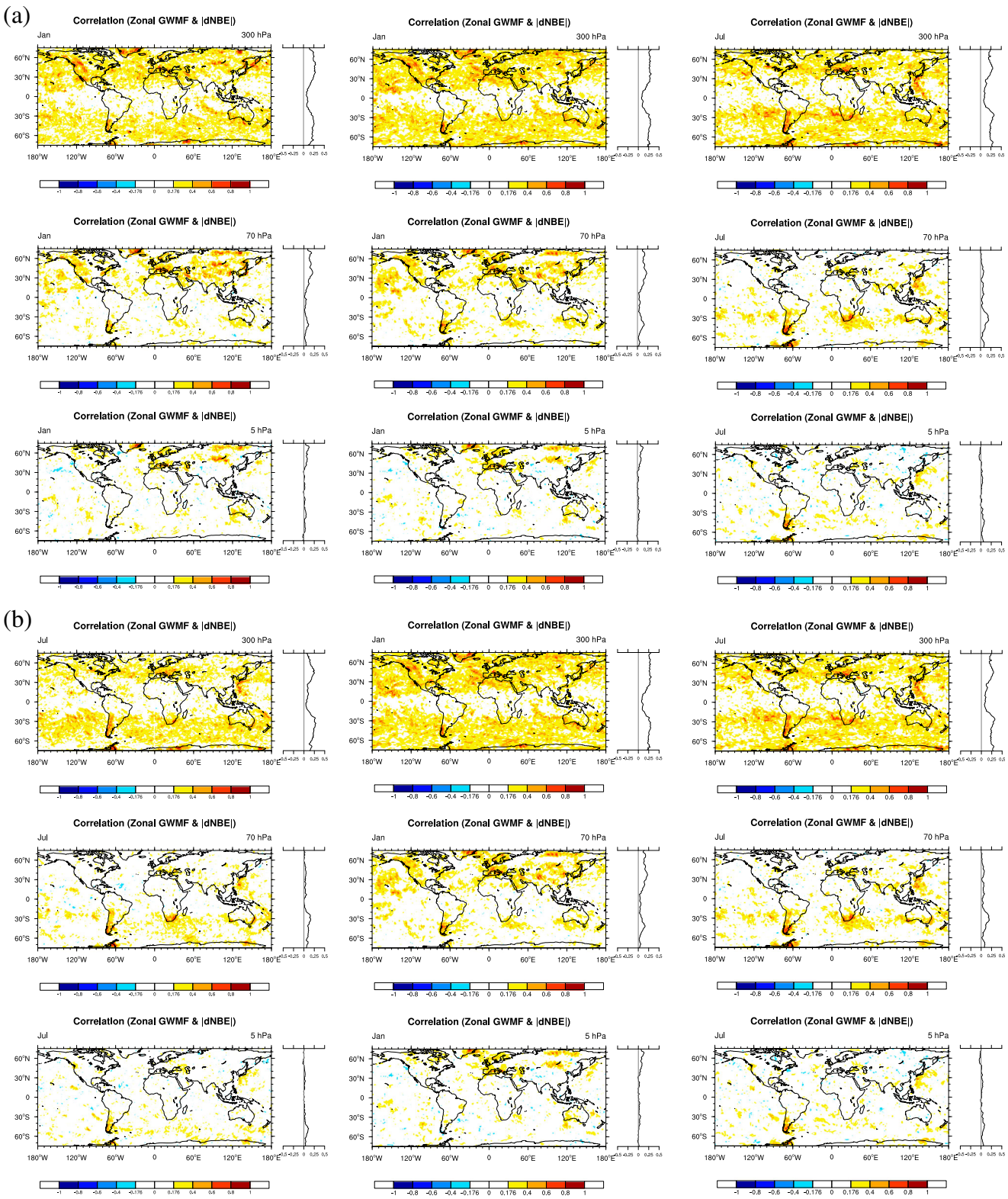

Fig. 13 The same as in Fig. 12, except for the correlation between RNBE and zonal GWMF

600 hPa, considering that GWs emerge somewhat higher than the actual surface front, which is located near ~800 hPa. On the other hand, RNBE is calculated at 350 hPa, which represents degree of imbalance of the large-scale flow near the upper-level jet of the troposphere. The feasibility of the two variables as the diagnostics of GWs associated with jet/front systems is examined by calculating the correlation coefficients between each variable and the GWMF estimated from high-resolution (0.25°

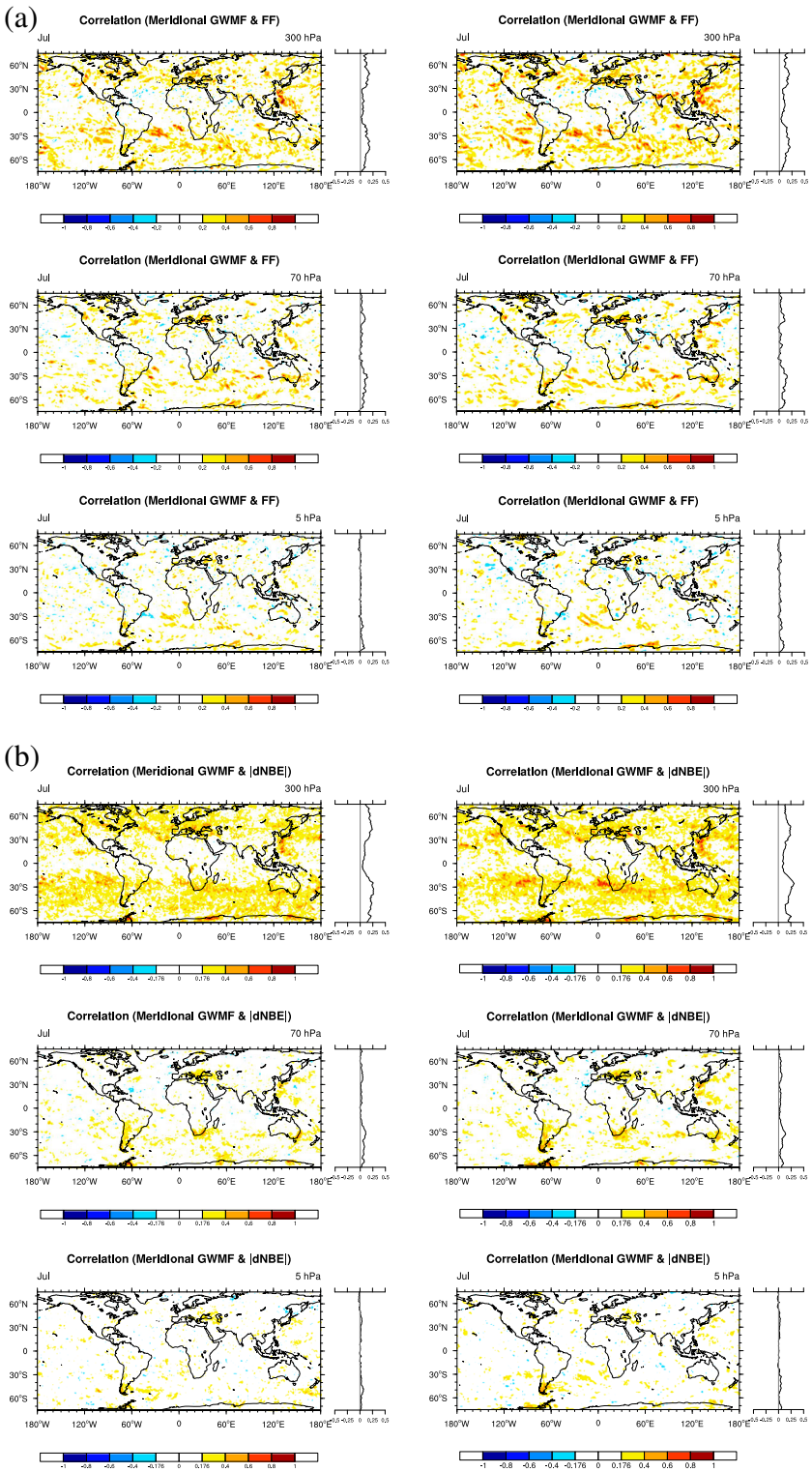

Fig. 14 Correlation between (**a**) the FF, which is calculated using MERRA (left) and ERA-Interim (right) data, and meridional GWMF estimated from high-resolution ECMWF analysis data in July of 2007. (**b**) The same as in (a) except for the correlation between RNBE and meridional GWMF

× 0.25°) ECMWF analysis data in January and July of 2007. The findings from the current study are as follows:

- The FF at 600 hPa and RNBE at 350 hPa are large poleward of 30° in both hemispheres, with local peaks near Greenland, East Asia, western North America, and the Andes Mountains.
- There is a clear seasonal march of the two diagnostics, with a maximum in winter and a minimum in summer, without significant interannual variations during the 32 years (1980–2011).
- The GWMF estimated from high-resolution ECMWF analysis data revealed that, in the upper troposphere, a

negative zonal momentum flux is dominant poleward of 30° in both hemispheres, with a larger value in the winter hemisphere, and that a weak positive zonal momentum flux exists in tropical and subtropical regions of the summer hemisphere. The meridional momentum flux is positive in the NH and negative in the SH for both seasons.

- The GWMF significantly decreases with height due to density reduction and filtering by the background wind, and consequently, a negative (positive) momentum flux is dominant in the mid-to-high latitudes of the winter hemisphere, while a positive (negative) momentum flux is dominant in the tropical and subtropical regions of the summer hemisphere for the zonal (meridional) momentum flux.
- The FF and RNBE are well correlated with GWMF in the mid-to-high latitudes of the upper troposphere, with local peaks near the southern tip of the Andes, North Africa and southern Europe, North America, and southern Australia. Although the correlations of the FF and RNBE with GWMF decrease at higher altitudes due to the filtering process, a strong correlation up to 5 hPa was sustained in some local regions of winter hemisphere, such as southwest Greenland and the southern Andes.
- The results of the current study demonstrate that the two diagnostics of GWs associated with jet/frontal systems, the FF and RNBE, are feasible for use as diagnostics of GWs in the parameterization, which can successfully separate GWs in the tropics and subtropics in the summer hemisphere generated by convective sources.

In Part II, we implement a new parameterization of a jet/front GWD scheme based on the RNBE into WACCM, and the impacts of the new scheme to large-scale circulation will be examined and compared with the original WACCM that includes the frontal GWD parameterization based on the FF.

Acknowledgements This work was supported by the R&D project on the development of global numerical weather prediction systems of the Korean Institute of Atmospheric Prediction Systems (KIAPS) funded by the Korean Meteorological Administration (KMA) and by the Korea Polar Research Institute (KOPRI, PE18020).

References

Alexander, M.J.: Global and seasonal variations in three-dimensional gravity wave momentum flux from satellite limb-sounding temperatures. Geophys. Res. Lett. **42**, 6860–6867 (2015). https://doi.org/10.1002/2015GL065234

American Meteorological Society: Glossary of meteorology. Allen Press. 855 (2000)

Andrews, D.G., Holton, J.R., Leovy, C.B.: Middle Atmosphere Dynamics. Academic Press, San Diego (1987) 489 pp

Butchart, N., Coauthors: Chemistry-climate model simulations of twenty-first century stratospheric climate and circulation changes. J. Clim. **23**, 5349–5374 (2010)

Charron, M., Manzini, E.: Gravity waves from fronts: parameterization and middle atmosphere response in a general circulation model. J. Atmos. Sci. **59**, 923–941 (2002)

Choi, H.-J., Chun, H.-Y.: Effects of vertical resolution on a parameterization of convective gravity waves. Atmosphere. **18**, 121–136 (2008)

Choi, H.-J., Han, J.-Y., Koo, M.-S., Chun, H.-Y., Kim, Y.-H., Hong, S.-Y.: Effects of non-orographic gravity wave drag on seasonal and medium-range predictions in a global forecast model. Asia-Pac. J. Atmos. Sci. **54**, 385–402 (2018)

Chun, H.-Y., Kim, Y.-H., Choi, H.-J., Kim, J.-Y.: Influence of gravity waves in the tropical upwelling: WACCM simulations. J. Atmos. Sci. **68**, 2599–2612 (2011)

Cohen, N.Y., Gerber, E.P., Bühler, O.: Compensation between resolved and unresolved wave driving in the stratosphere: implications for downward control. J. Atmos. Sci. **70**, 3780–3798 (2013)

Dee, D.P., Coauthors: The ERA-interim reanalysis: configuration and performance of the data assimilation system. Quart. J. Roy. Meteor. Soc. **137**, 553–597 (2011)

Eckermann, S., Vincent, R.: VHF radar observations of gravity-wave production by cold fronts over southern Australia. J. Atmos. Sci. **50**, 785–806 (1993)

Ern, M., Preusse, P., Gille, J., Hepplewhite, C., Mlynczak, M., Russell III, J., Riese, M.: Implications for atmospheric dynamics derived from global observations of gravity wave momentum flux in stratosphere and mesosphere. J. Geophys. Res. **116**, D19107 (2011). https://doi.org/10.1029/2011JD015821.

Ford, R., McIntyre, M., Norton, W.: Balance and the slow quasimanifold: some explicit results. J. Atmos. Sci. **57**, 1236–1254 (2000)

Fritts, D., Alexander, J.: Gravity wave dynamics and effects in the middle atmosphere. Rev. Geophys. **41**(1), 1003 (2003). https://doi.org/10.1029/2001RG000106.

Fritts, D., Nastrom, G.: Sources of mesoscale variability of gravity waves. Part II: frontal, convective, and jet stream excitation. J. Atmos. Sci. **49**, 111–127 (1992)

Garcia, R., Boville, B.: Downward control of the mean meridional circulation and temperature distribution of the polar winter stratosphere. J. Atmos. Sci. **51**, 2238–2245 (1994)

Griffiths, M., Reeder, M.J.: Stratospheric inertia-gravity waves generated in a numerical model of frontogenesis. I: Model solutions. *Quart. J. Roy. Soc.* **122**, 1153–1174 (1996)

Guest, F., Reeder, M., Marks, C., Karoly, D.: Inertia-gravity waves observed in the lower stratosphere over Macquarie Island. J. Atmos. Sci. **57**, 737–752 (2000)

Hertzog, A., Boccara, G., Vincent, R., Vial, F., Coquerez, P.: Estimation of gravity-wave momentum fluxes and phase speeds from long-duration stratospheric balloon flights. 2. Results from the Vorcore campaign in Antarctica. J. Atmos. Sci. **65**, 3056–3070 (2008)

Holton, J.R.: An Introduction to Dynamic Meteorology. Academic Press (1992) 535 pp

Hoskins, B.J.: The mathematical theory of frontogenesis. Ann. Rev. Fluid Mech. **14**, 131–151 (1982)

Jia, J.Y., Preusse, P., Ern, M., Chun, H.-Y., Gille, J.C., Eckermann, S.D., Riese, M.: Sea surface temperature as a proxy for convective gravity wave excitation: a study based on global gravity wave observation in the middle atmosphere. Ann. Geophys. **32**, 1373–1394 (2014)

Kang, M.-J., Chun, H.-Y.: Momentum flux of convective gravity waves derived from an offline gravity wave parameterization. Part I: spatiotemporal variations at source level. J. Atmos. Sci. **74**, 3167–3187 (2017)

Ki, M.-O., Chun, H.-Y.: Inertia-gravity waves associated with deep convection observed during the summers of 2005 and 2007 in Korea. J. Geophys. Res. **116**, D16122 (2011). https://doi.org/10.1029/2011JD015684.

Kim, S.-Y., Chun, H.-Y.: Momentum flux of stratospheric gravity waves generated by typhoon Ewiniar (2006). Asia-Pacific J. Atmos. Sci. **46**, 199–208 (2010)

Kim, J.-H., Chun, H.-Y., Sharman, R.D., Keller, T.L.: Evaluations of upper-level turbulence diagnostics performance using the graphical turbulence guidance (GTG) system and pilot reports (PIREPs) over East Asia. J. Appl. Meteor. Climatol. **50**, 1936–1951 (2011)

Kim, Y.-H., Chun, H.-Y., Preusse, P., Ern, M., Kim, S.-Y.: Gravity wave reflection and its influence on the consistency of temperature- and wind-based momentum fluxes above typhoon Ewiniar. Atmos. Chem. Phys. **12**, 10787–10795 (2012)

Kim, Y.-H., Chun, H.-Y., Park, S.-H., Song, I.-S., Choi, H.-J.: Characteristics of gravity waves generated in the jet-front system in a baroclinic instability simulation. Atmos. Chem. Phys. **16**, 4799–4815 (2016)

Lane, T.P., Knievel, J.C.: Some effects of model resolution on simulated gravity waves generated by deep, mesoscale convection. J. Atmos. Sci. **62**, 3408–3419 (2005)

Limpasuvan, V., Alexander, M.J., Orsolini, Y.J., Wu, D.L., Xue, M., Richter, J.H., Yamashita, C.: Mesoscale simulations of gravity waves during the 2008-2009 major stratospheric sudden warming. J. Geophys. Res. **116**, D17104 (2011). https://doi.org/10.1029/3010JD015190.

Lindzen, R.S.: Turbulence and stress owing to gravity wave and tidal breakdown. J. Geophys. Res. **86**, 9707–9714 (1981)

Liu, H.-L., McInerney, J.M., Santos, S., Lauritzen, P.H., Taylor, M.A., Pedatella, N.M.: Gravity waves simulated by high-resolution whole atmosphere community climate model. Geophys. Res. Lett. **41**, 9106–9112 (2014). https://doi.org/10.1002/2014GL062468

Mirzaei, M., Zülicke, C., Mohebalhojeh, A.R., Ahmadi-Givi, F., Pluogonven, R.: Structure, energy, and propagation of inertia-gravity waves in dray and moist simulation of a baroclinic wave life cycle. J. Atmos. Sci. **71**, 2390–2414 (2014)

Moore, J.T., Abeling, W.A.: A diagnosis of unbalanced flow in upper levels during the AVE-SESAME I period. Mon Wea. Rev. **116**, 2425–2436 (1988)

Murphy, D.J., Alexander, S.P., Klekociuk, A.R., Love, P.T., Vincent, R.A.: Radiosonde observations of gravity waves in the lower stratosphere over Davis, Antarctica. J. Geophys. Res. **119**, 11,973–11,996 (2014). https://doi.org/10.1002/2014JD022448

O'Sullivan, D., Dunkerton, T.: Generation of inertia-gravity waves in a simulated life-cycle of baroclinic instability. J. Atmos. Sci. **52**, 3695–3716 (1995)

Persson, A., Grazzini, F.: User guide to ECMWF forecast products. Meteorol. Bull. **M3**, 2 (2005) 161pp

Plougonven, R., Snyder, C.: Inertia-gravity waves spontaneously generated by jets and fronts. Part I: different baroclinic life cycles. J. Atmos. Sci. **64**, 2502–2520 (2007)

Plougonven, R., Teitelbaum, H.: Comparison of a large-scale inertia-gravity wave as seen in the ECMWF and from radiosondes. Geophys. Res. Let. **30**(18), 1954 (2003). https://doi.org/10.1029/2003GL017716

Plougonven, R., Zhang, F.: Internal gravity waves from atmospheric jets and fronts. Rev. Geophys. **52**, 33–76 (2014)

Polichtchouk, I., Shepherd, T.G., Hogan, R.J., Bechtold, P.: Sensitivity of the brewer–Dobson circulation and polar vortex variability to parameterized nonorographic gravity wave drag in a high-resolution atmospheric model. J. Atmos. Sci. **65**, 1525–1542 (2018)

Preusse, P., Ern, M., Bechtold, P., Eckermann, S.D., Kalisch, S., Trinh, Q.T., Riese, M.: Characteristics of gravity waves resolved by ECMWF. Atmos. Chem. Phys. **14**(19), 10483–10508 (2014)

Randel, W.J., Garcia, R.R., Wu, F.: Dynamical balances and tropical stratospheric upwelling. J. Atmos. Sci. **65**, 3584–3595 (2008)

Réchou, A., Kirkwood, S., Arnault, J., Dalin, P.: Short vertical-wavelength inertia-gravity waves generated by a jet-front system at Arctic latitudes-VHF radar. radiosondes and numerical modeling. *Atmos. Chem. Phys*. **14**, 6785–6799 (2015)

Richter, J.H., Sassi, F., Garcia, R.R.: Toward a physically based gravity wave source parameterization in a general circulation model. J. Atmos. Sci. **67**, 136–156 (2010)

Richter, J.H., Solomon, A., Bacmeister, J.T.: On the simulation of the quasi-biennial oscillation in the community atmosphere model. Version 5. *J. Geophys. Res.* **119**, 3045–3062 (2014)

Rienecker, M.M., Coauthors: MERRA: NASA's modern-era retrospective analysis for research and applications. J. Clim. **24**, 3624–3648 (2011)

Sato, K.: A statistical study of the structure, saturation and sources of inertio-gravity waves in the lower stratosphere observed with the MU radar. J. Atmos. Terr. Phys. **56**(6), 755–774 (1994)

Sato, K., Yoshiki, M.: Gravity wave generation around the polar vortex in the stratosphere revealed by 3-hourly radiosonde observations at Syowa Station. J. Atmos. Sci. **65**, 3719–3735 (2008)

Sato, K., Tateno, S., Watanabe, S., Kawatani, Y.: Gravity wave characteristics in the southern hemisphere revealed by a high-resolution middle-atmosphere general circulation model. J. Atmos. Sci. **69**, 1378–1396 (2012)

Sharman, R., Tebaldi, C., Wienner, G., Wolff, J.: An integrated approach to mid- and upper-level turbulence forecasting. Wea. Forecasting. **21**, 268–287 (2006)

Sharman, R.D., Doyle, J.D., Shapiro, M.A.: An investigation of a commercial aircraft encounter with severe clear-air turbulence over western Greenland. J. Appl. Meteor. Climatol. **51**, 42–53 (2012)

Shutts, G., Vosper, S.: Stratospheric gravity waves revealed in NWP forecast models. Q. J. R. Meteorol. Soc. **137**(655), 303–317 (2011)

Song, I.-S., Lee, C., Kim, J.-H., Jee, G., Kim, Y.-H., Choi, H.-J., Chun, H.-Y., Kim, Y.-H.: Meteor radar observations of vertically propagating low-frequency inertia-gravity waves near the southern polar mesopause region. J. Geophys. Res. Space Physics. **122**, 4777–4800 (2017). https://doi.org/10.1002/2016JA022978

Uccelini, L., Koch, S.: The synoptic setting and possible energy sources for mesoscale wave disturbances. Mon. Wea. Rev. **115**, 721–729 (1987)

Untch, A., M. Miller, M. Hortal, R. Buizza, and P. Janssen, 2006: Towards a global meso-scale model: The high-resolution system T799L91 and T399L62EPS. *Newsl*. **108**, pp. 6–13, Eur. Cent. for Medium-Range Weather Forecast., Reading, U. K.

Wang, L., Geller, M.: Morphology of gravity-wave energy as observed from 4 years (1998–2001) of high vertical resolution U.S. radiosonde data. J. Geophys. Res. **108**, ACL 1-1–ACL 1-12 (2003). https://doi.org/10.1029/2002JD002786

Wang, S., Zhang, F.: Sensitivity of mesoscale gravity waves to the baroclinicity of jet-front systems. Mon. Wea. Rev. **135**, 670–688 (2007)

Wang, S., Zhang, F.: Source of gravity waves within a vortex-dipole jet revealed by a linear model. J. Atmos. Sci. **67**, 1438–1455 (2010)

Wu, D., Eckermann, S.: Global gravity wave variances from Aura MLS: characteristics and interpretation. J. Atmos. Sci. **65**, 3695–3718 (2008)

Wu, D., Zhang, F.: A study of mesoscale gravity waves over the North Atlantic with satellite observations and a mesoscale model. J. Geophys. Res. **109**, (2004). https://doi.org/10.1029/2004JD005.090.

Yoo, J.-H., Choi, T., Chun, H.-Y., Kim, Y.-H., Song, I.-S., Song, B.-G.: Inertia-gravity waves revealed in radiosonde data at Jang Bogo Station Antarctica (74°37'S, 164°13′E). Part I: characteristics, energy, and momentum flux. J. Geophys. Res. (2018) in press

Zhang, F.: Generation of mesoscale gravity waves in upper-tropospheric jet-front systems. J. Atmos. Sci. **61**(4), 440–457 (2004)

Zhang, S., Yi, F.: Latitudinal and seasonal variations of inertial gravity wave activity in the lower atmosphere over Central China. J. Geophys. Res. **112**, D05109 (2007). https://doi.org/10.1029/2006JD007487

Zhang, F., Koch, S., Davis, C., Kaplan, M.: Wavelet analysis and the governing dynamics of a large amplitude mesoscale gravity wave event along the east coast of the United States. Q. J. R. Meteorol. Soc. **127**, 2209–2245 (2001)

Zhang, F., Zhang, M., Wei, J., Wang, S.: Month-long simulations of gravity waves over North America and 6 North Atlantic in comparison with satellite observations. Acta Meteorol. Sin. **27**, 446–454 (2013). https://doi.org/10.1007/s13351-013-0301-x